Quantifying and Characterizing Striping of Microwave Humidity Sounder with Observation and Simulation

John Xun Yang, *Senior Member, IEEE*, Yalei You, William Blackwell, *Fellow, IEEE*, Sidharth Misra, *Senior Member, IEEE*, Rachael A. Kroodsma

Abstract—Striping has been observed in the MetOp-A Microwave Humidity Sounder (MHS) data since its degradation in November 2018. However, accurate striping quantification and characterization remain challenging due to the large scene dynamics observed at W/G bands of MHS. Here we have developed a set of novel algorithms for striping quantification, decomposition, characterization, and simulation. Our algorithm extracts striping from the warm-load and cold-space scenes that are relatively stable. We break down the striping into two parts of thermal and $1/f$ noise and quantify their absolute magnitude and relative ratio. We found a significant increase in striping at 157 GHz that has more than quadrupled by October 2019 relative to its normal level. Regardless of the degradation, the ratio of thermal and $1/f$ noise remains the same. Our simulation reproduces all the characteristics of striping against observation. It is shown that $1/f$ noise generates sharp, non-periodic stripes, while thermal noise also generates stripes but with smoother band features. The latter is due to the periodic calibration that has a chopping effect. The striping percentage, defined as the ratio of 1/f to total noise, shows no dependence on the scene temperature. Striping is pronounced not only in 157 GHz but also in 89 and 190 GHz with the striping percentage over 50%, while lower in 183 GHz of 20%. The results provide insights for quantifying and understanding striping. Our algorithm can be applied to other radiometers and to simulate striping for evaluating its impact in data assimilation and science products.

Index Terms—Microwave radiometry, Striping, $1/f$ noise, Thermal noise, Satellites

I. INTRODUCTION

Striping is a distinctive radiometric feature that has been found in many microwave radiometers [1]–[7]. Striping exhibits itself as sharp, non-periodic stripe patterns with large fluctuation in both radiance data and high-level science products. Stripes appear directional in the cross-track direction (along-scan) rather than along-track. It is also referred to as stripes or striping noise. Striping is not only found in ground tests and in-orbit operations [2], [4], [7], [8], but also in data assimilation for numerical weather prediction (NWP) modeling [5], [9]. While thermal noise has a stationary mean, striping appears non-stationary, which can severely degrade radiometer performance and data applications. Striping detection and quantification are important for assessing hardware performance and quantifying radiometric uncertainty propagation through data assimilation and weather forecast [10], [11].

The detection and quantification of striping for W/G bands are challenging due to the naturally occurring large dynamics of brightness temperature (T_B) at these channels. The Microwave Humidity Sounder (MHS) contains five channels at W/G bands [12]. The 89 GHz at W-band is for measuring surface water vapor, and the four channels at G-band (157-190 GHz) are for atmospheric sounding. These channels exhibit strong T_B dynamic behavior, which is hard to accurately simulate with a radiative transfer model (RTM) and reanalyses [13]–[15]. The observed minus simulated T_B yields pronounced residual errors that mask the striping signal and prohibits the accurate striping quantification. This is in contrast to V-band channels for sounding upper atmosphere since V-band T_B has less spatiotemporal variation and can be modeled with relatively higher accuracy for striping detection [5], [9]. While challenges are present, it is worthwhile to develop algorithms for quantifying and characterizing striping of W/G bands since these channels are indispensable for humidity and troposphere sounding [14]–[16]. New W/G band radiometers onboard small satellites are emerging, such as the Time-Resolved Observations of Precipitation structure and storm Intensity with a Constellation of Smallsats (TROPICS) and the Temporal Experiment for Storms and Tropical Systems - Demonstration (TEMPEST-D) [17], [18]. These CubeSat constellations employ substantial technology advancements, so it is vital to develop new algorithm for striping quantification and hardware performance assessment.

In addition to striping detection and quantification, the composition and cause of striping need investigation. Striping is often attributed to the presence of $1/f$ noise [2], [4], [7], [8]. $1/f$ noise is intrinsic in semiconductor components of the radio frequency integrated circuit (RFIC) of microwave radiometers [19], [20]. Additionally, periodic calibrations are widely implemented for scanning radiometers to reduce the
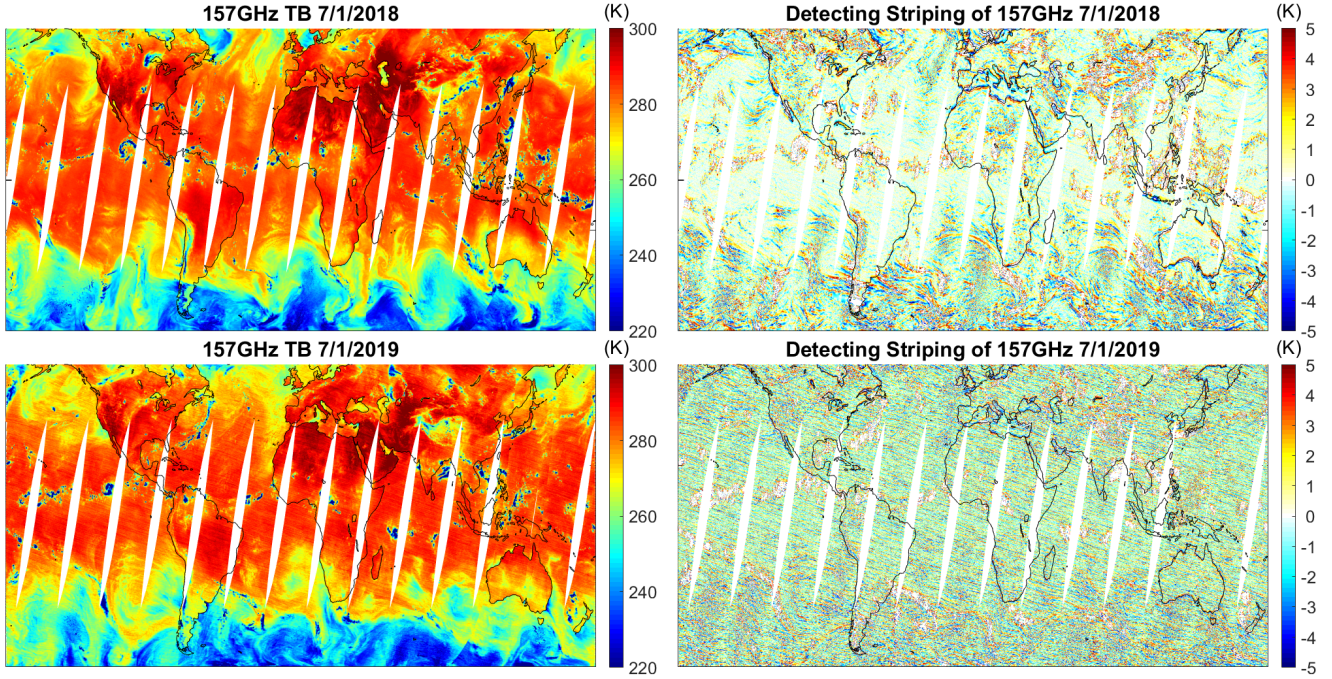
Fig. 1. Striping at 157 GHz of MetOp-A MHS. Striping became remarkable on July 1st, 2019, compared to one year ago. (Lower right) Obvious cross-track stripes show up in a 10-K colorbar range with a high-pass filter that removes the background variations. (Lower left) Striping is so significant that it can be perceived in the Earth scene map that has a T_B range of 80 K (Zoom in as appropriate).

gain instability [21], [22]. The periodic calibration has a *chopping effect* such that calibration can only be conducted every a few seconds. This results in discontinuity and such effect should be evaluated. It would be very useful to reproduce striping through simulation. Simulation can differentiate the impact of different factors that are often blended. Simulation also complements observation that has considerable measurement uncertainties, particularly at W/G bands. With simulation, striping can be generated for studying its propagation and impact in science products and data assimilation of NWP model [5], [11], [14].

The MetOp-A MHS 157 GHz channel has shown remarkable striping since its degradation in November 2018. Figure 1 shows the striking striping of a 10-K range in July 2019 with a high-pass filter. The filter removes the scene variation by applying a moving-average for brightness temperature of every 10 along-track scans and subtracting the averaged brightness temperature from the original ones. However, an accurate striping quantification is still difficult due to Earth scene dynamics that produces large uncertainties after applying the high-pass filter [14], [15], [23]. Here we have developed a set of novel algorithms for quantifying and simulating striping and applied it to MHS. The rest of the paper is organized as follows. First, we introduce the algorithms on striping simulation, quantification, and decomposition in Section II. Section III presents the results of both simulation and observation. We validate our simulation against observation with spectral analysis and eigen-decomposition. The striping of MHS is quantified, decomposed, and characterized. We have examined the striping dependence on scene temperature and its temporal variability. Conclusion and discussion are present in the last
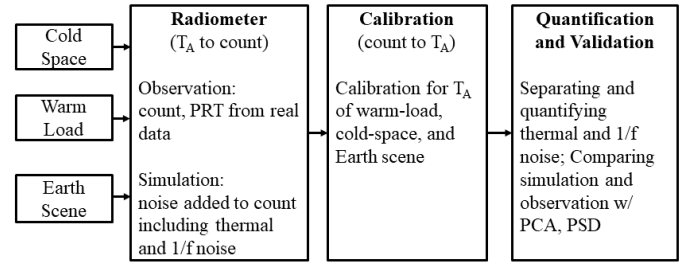
Fig. 2. Overview of implementing and comparing simulation and observation. A set of algorithms are developed for striping simulation, quantification, and validation.

section.

II. ALGORITHMS OF SIMULATION AND OBSERVATION

Figure 2 shows the overview of the algorithm structure. Both simulation and observation follows the same diagram that illustrates a typical radiometer. The algorithms we developed encompasses three parts of striping simulation, quantification, and validation. They are detailed in the following three sections.

A. Simulating Striping

A simplified formula for the measured count of a radiometer can be written as [24]

$$C = (T_A + T_R)G \tag{1}$$

where C is the uncalibrated measured radiometer count, T_A is the antenna temperature, T_R is the receiver temperature, and

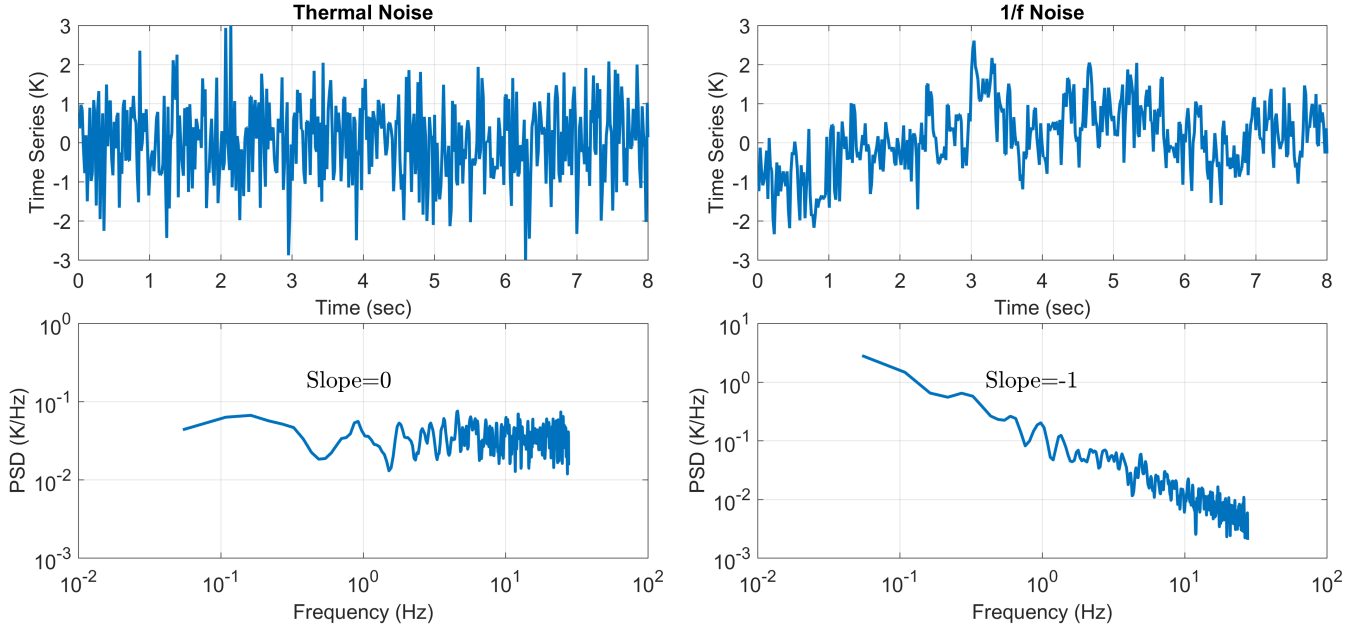Fig. 3. Time series and power spectral density of simulated thermal and $1/f$ noise with a standard deviation of 1 K. $1/f$ noise has a non-stationary mean with remarkable fluctuations in the time domain, and its power-law slope is -1 in the PSD.

G is the power gain of the radiometer. The system temperature can be defined as $T_{sys} = T_A + T_R$. In the presence of noise or unwanted signals, Equation 1 can be written as

$$C = (T_A + T_R + \sum n_i)G \qquad (2)$$

where n_i represents a number of individual noise or unwanted signals. The short-term gain fluctuation can be implicitly counted as an individual n_i. The long-term gain and receiver oscillations due to the orbital variation are different from short-term fluctuation, and we will introduce them shortly in this section.

With regard to the n_i, we focus on the thermal noise and $1/f$ noise. Thermal noise is due to the random motion of agitated charge carriers and is universal in all electronic devices [19], [20]. An additive model is used to generate thermal noise. We assume thermal noise is additive white Gaussian noise (AWGN) [25]. AWGN is generated by a pseudo random number generator (RNG) of the Mersenne Twister RNG, and it is assumed to be zero-mean and wide-sense stationary with a flat spectrum [26].

$1/f$ noise is also called flicker noise or excess noise. It can arise from different mechanisms. It is pronounced in electronics sensitive to surface phenomenon related to charge trapping and releasing and carrier generation and recombination [1], [19]. $1/f$ noise exhibits a spectral slope in the power spectral density (PSD) and is produced with the Fast Fourier Transform (FFT) [27], [28]. We first generate thermal noise in the time domain and then apply FFT transform

$$h(\omega) = \mathcal{F}\{n_{\text{thermal}}(t)\} \qquad (3)$$

where $n_{\text{thermal}}(t)$ is thermal noise in the time domain, and $h(\omega)$ is its Fourier transform.

In order to generate 1/f noise, the thermal noise $h(\omega)$ is multiplied with a term to tune the power-law slope. Then, the inverse FFT is applied to get back to the time domain

$$n_{1/f}(t) = \mathcal{F}^{-1}\{h(\omega)f^{\frac{\alpha}{2}}\} \qquad (4)$$

where $n(t)$ is the noise we want, and f is the frequency. $\alpha/2$ is the power law exponent, and the constant 2 in the denominator accounts for the fact that power spectrum is the square of Fourier transform. For $1/f$ noise, $\alpha = -1$. The method can also be used to generate other noise with different α such as quantization [28]. Figure 3 shows simulated thermal and 1/f noise with a standard deviation of 1 K. 1/f noise has a power-law slope of -1 in the PSD, while thermal noise has a flat spectrum. The time series of 1/f noise show remarkable fluctuations with non-stationary mean. On the other hand, thermal noise has a stationary mean despite fluctuations.

The generated thermal and $1/f$ noises, n_{thermal} and $n_{1/f}$, are blended for the total noise n_{total}

$$n_{\text{total}} = n_{\text{thermal}} + n_{1/f} \qquad (5)$$

The individual noise magnitude can be tuned for specific simulation, and the total magnitude follows

$$\sigma_{\text{total}}^2 = \sigma_{\text{thermal}}^2 + \sigma_{1/f}^2 \qquad (6)$$

where σ_{total}, σ_{thermal}, and $\sigma_{1/f}$ are the standard deviation of the total, thermal, and $1/f$ noise, respectively.

The payload environment usually has an orbital oscillation as the spacecraft orbits the Earth [13], [28]–[31]. It is due to the change of solar incidence angle and environment temperature along the orbit. The radiometer gain and warm-load temperature oscillate with a period same as the spacecraft

orbital period [28]. For MHS, the orbital period is ~ 100 minutes. The orbital oscillation can be described as

$$
\begin{aligned}
T_W &= T_{W0} + \Delta T_W(t, \lambda, a, \phi) \\
G &= G_0 + \Delta G(t, \lambda, a, \phi)
\end{aligned}
\quad (7)
$$

where T_{W0} and G_0 are constant, and ΔT_W and ΔG are oscillation in terms of waveform as a function of time t, wavelength λ, amplitude a, and phase ϕ. A variety of waveforms can be simulated. We can also import empirical orbital oscillations from observations as the oscillation term. In this study, we use sinusoidal wave with the empirical magnitudes from observation [29].

A radiometer observes both the cold and warm reference targets and the Earth scene during one complete rotation of the reflector. We generate counts as follows

$$
\begin{aligned}
C_W &= (T_{A,W} + T_R + n_W)G \\
C_C &= (T_{A,C} + T_R + n_C)G \\
C_S &= (T_{A,S} + T_R + n_S)G
\end{aligned}
\quad (8)
$$

where $T_{A,W}$, $T_{A,C}$, and $T_{A,S}$ are the warm-load, cold-space, and Earth scene temperature, respectively. n_W, n_C, and n_S are corresponding noise, and C_C, C_W, C_S are counts. If the warm-load is a perfect blackbody, there is $T_{A,W} = T_W$. And $T_{A,C}$ equals the cosmic temperature T_C, if the cold-space view has no contamination from the reflector emission or field of view (FOV) intrusion.

During one complete $360°$ rotation of the reflector spin, MHS has a duty cycle of 65% for the cold and warm targets and the Earth scene. This duty cycle has a conditional sampling effect, and to account for it, we also simulate the null count of the other 35% measuring time as

$$
C_N = (T_{A,N} + T_R + n_N)G \quad (9)
$$

where C_N, $T_{A,N}$, and n_N denote the null count, scene temperature, and noise, respectively. The null simulation is not used but better represents MHS work mode of a conditional sampling.

$T_{A,S}$ is calibrated from the measured counts

$$
T_{A,S} = \frac{(T_W - T_C)}{(C_W - C_C)}(C_S - C_C) + T_C \quad (10)
$$

Given the antenna temperature T_A, brightness temperature T_B can be derived with the antenna pattern correction (APC). APC is not considered here, and T_A and T_B are exchangeable hereafter. The presence of noise will propagate into the calibrated scene temperature, as shown in following sections.

B. Quantifying Striping

Rather than dealing with the dynamic Earth scene, we quantify striping from the warm-load and cold-space that are much more stable [28]. The algorithm of using warm-load and cold-space from in-orbit measurement shows agreement against the ground test [28]. The warm-load temperature is measured by the onboard platinum resistance thermometer (PRT), and the cold-space cosmic temperature can be considered constant.

The warm-load antenna temperature $T_{A,W}$ is given by

$$
T_{A,W i,j} = \frac{1}{\overline{G_j}}(C_{W i,j} - \overline{C_{C j}}) + T_C, \quad 2 \leq i \leq 4 \quad (11)
$$

where $C_{W i,j}$ is the warm-load count as a function of scan positions in terms of cross-track i and along-track j. $\overline{C_{C j}}$ and $\overline{G_j}$ are the smoothed cold count and gain respectively, and they are only dependent on along-track positions after smoothing. T_C is a constant for the cosmic temperature. It is noted that i ranges from 2 to 4 for $C_{W i,j}$. MHS has 4 scans for the warm-load and cold-space respectively each spin. We only use scans 2-4 for deriving the warm-load T_A, while scan-1 is used for deriving the gain as follows. This can avoid producing pseudo signals of f^2 spectra that comes from blending the gain and scene temperature derivation [28]. Data of one orbit can be used with around 2400 along-track scanlines for MHS.

$\overline{G_j}$ is given by

$$
\overline{G_j} = \frac{\overline{C_{W i,j}} - \overline{C_{C j}}}{\overline{T_{W j}} - T_C}, \quad i = 1 \quad (12)
$$

It is noted that the first cross-track sample of $C_{W i,j}$ is used for deriving the gain.

The cold count is smoothed as

$$
\overline{C_{C j}} = \frac{1}{4L} \sum_{k=j-\frac{(L+1)}{2}}^{j+\frac{(L+1)}{2}} w_k \sum_{i=1}^{4} C_{C i,j} \quad (13)
$$

where w_k is a window function with L as the window length. For MHS, a triangular window of $L = 7$ has been used with the window length optimized in the ground test [12]. We use all the four cross-track samples for smoothing the cold count since we are to derive the warm-load $T_{A,W}$.

The warm-load PRT temperature is smoothed as

$$
\overline{T_{W j}} = \frac{1}{L} \sum_{k=j-\frac{(L+1)}{2}}^{j+\frac{(L+1)}{2}} w_k T_{W j} \quad (14)
$$

The warm-load count is smoothed as

$$
\overline{C_{W i,j}} = \frac{1}{L} \sum_{k=j-\frac{(L+1)}{2}}^{j+\frac{(L+1)}{2}} w_k \sum_{i=1}^{1} C_{W i,j}, \quad i = 1 \quad (15)
$$

where there is $i = 1$ since the other 3 scans are used for deriving warm-load $T_{A,W}$.

The warm-load antenna temperature $T_{A,W}$ has orbital oscillations, which can be removed with measurements from the warm-load PRT

$$
n_{A,W i,j} = T_{A,W i,j} - \overline{T_{W j}}, \quad 2 \leq i \leq 4 \quad (16)
$$

where $n_{A,W}$ is the residual warm-load noise that contains thermal and striping noise. It has 3 cross-track samples and 2400 along-track scans of one orbit for MHS.

The one-sided PSD of the warm-load noise $n_{A,W}$ can be written as

$$
S(f) = \mathcal{F}^2\{n_{A,W}\} \quad (17)
$$

where $S(f)$ is the one-sided PSD of the square of Fourier transform. The warm-load noise $n_{A,W}$ is reshaped to one-dimensional vector ingested to Fourier transform. The entries of the 1-D vector are ordered in time series such that the first measured samples are put at the beginning.

The magnitude of the total noise is determined as

$$\text{NEDT}_{\text{total}} = \sqrt{\int_{f_{dn}}^{f_{up}} S(f) df} \tag{18}$$

where $\text{NEDT}_{\text{total}}$ is the Noise Equivalent Delta Temperature (NEDT) of the total noise, f_{dn} is the lower bound of the frequency, f_{up} is the upper bound which is the Nyquist frequency.

NEDT of total noise is also equivalent to the unbiased second central moment of noise in the time domain [28]

$$\text{NEDT}_{\text{total}} = \sqrt{\frac{1}{NM-1} \sum_{j=1}^{N} \sum_{i=1}^{M} (n_{A,W_{i,j}} - \overline{n_{A,W}})^2} \tag{19}$$

where M and N are numbers of cross-track and along-track of noise respectively, and $\overline{n_{A,W}} = \frac{1}{MN} \sum_{j=1}^{N} \sum_{i=1}^{M} n_{A,W_{i,j}}$. For MHS, there are $M = 3$ and $N = 2400$ for one orbit. NEDT is the same from the time and frequency domain methods per Parseval's theorem. The frequency domain method can denote the spectral range of thermal and $1/f$ noise.

Thermal noise is the integration of PSD of high-frequency regimes

$$\text{NEDT}_{\text{thermal}} = \sqrt{\frac{(f_{up} - f_{dn})}{(f_{up} - f_m)} \int_{f_m}^{f_{up}} S(f) df} \tag{20}$$

where f_m is the tie point for separating thermal noise (high-frequency regimes) and $1/f$ noise (low-frequency regimes). We set the f_m as 18.5 Hz for MHS. This is because we get three cross-track samples for $T_{A,W}$ per rotation. The adjacent cross-track samples have a time interval of 0.018 second, and thus there is $1/(0.018 \times 3) = 18.5$. The above equation counts high-frequency noise of $f > 18.5$ Hz as thermal noise. Thermal noise is dominant at the high-frequency regime (small time scale), while $1/f$ noise plays a role in the low-frequency regime [1], [19].

Alternatively, thermal noise can be calculated in the time domain

$$\text{NEDT}_{\text{thermal}} = \sqrt{\frac{1}{2N(M-1)} \sum_{j=1}^{N} \sum_{i=1}^{M-1} (n_{A,W_{i+1,j}} - n_{A,W_{i,j}})^2} \tag{21}$$

Noise of adjacent cross-track samples of 0.018 second are counted as thermal noise since thermal noise is dominant at the small time scale (high-frequency). This method operates in the time domain and produces similar but more stable results compared to the PSD method since it avoids the spectral leakage of PSD [32]. This time domain method is based on Allan variance since Allan variance can provide an unbiased estimate of thermal noise [28]. But the PSD method has a clear mathematical expression that indicates the spectra range of thermal noise.

$1/f$ noise is given by

$$\text{NEDT}_{1/f} = \sqrt{(\text{NEDT}_{\text{total}}^2 - \text{NEDT}_{\text{thermal}}^2)} \tag{22}$$

We define the *striping percentage* or *1/f percentage*, as

$$P_{1/f} = \frac{\text{NEDT}_{1/f}^2}{\text{NEDT}_{\text{total}}^2} \times 100\% \tag{23}$$

$P_{1/f}$ ranges from 0 to 100%. This is a useful metric for quantifying striping as it has a clear physical meaning with a normalized range. If there is only thermal noise, $P_{1/f} = 0$. With the striping percentage, different channels and sensors can be compared.

Another useful index, *striping ratio*, can be defined as

$$R_{1/f} = \frac{\text{NEDT}_{1/f}}{\text{NEDT}_{\text{thermal}}} \tag{24}$$

The striping ratio compares the $1/f$ noise against thermal noise. $R_{1/f} = 0$ denotes no $1/f$ noise, and $R_{1/f} = 1$ means that thermal noise is equivalent to $1/f$ noise.

The steps introduced above are for studying striping with the warm-load scenes. The same procedure can be implemented for the cold-space scenes. Since there is a big difference of in the scene temperature between the cold-space (~ 3K) and warm-load (~ 280K), the scene-dependence can be studied by comparing them.

C. Validation and Principal Component Analysis

We have compared the simulation with observation in time and frequency domain. We also have applied principal component analysis (PCA) to analyze the data. PCA provides an different angle for characterizing striping compared to the time series and frequency domain analyses. PCA can differentiate 1/f noise from thermal noise by decomposing data in the empirical orthogonal basis. When two channels have close but nonidentical striping percentage, it is difficult to differentiate them with PSD since PSD is often very noisy due to the spectral leakage [32]. PCA can provide the explained variance that is much less noisy to discern the channel difference.

The brightness temperature or noise can be written as

$$A = \begin{bmatrix} x_{1,1} & \cdots & x_{1,n} \\ \vdots & \ddots & \vdots \\ x_{m,1} & \cdots & x_{m,n} \end{bmatrix} \tag{25}$$

where the rows are for cross-track with the columns for the along-track. We remove the columnar mean of A so that A has zero mean for each column. Its covariance matrix is

$$C = \frac{1}{(n-1)} A^T A \tag{26}$$

PCA can be solved by the eigen-decomposition of the covariance matrix

$$C = E \Lambda E^T \tag{27}$$

where E is the eigenvector matrix with columns as eigenvectors, and Λ is a diagonal matrix of variance.

However, the covariance matrix size is the square of the along-track number n and becomes computationally difficult to solve with a large n. In practice, we solve PCA with the single value decomposition (SVD). SVD does not need to construct the covariance matrix. Also, SVD can solve for the first few eigenvectors rather than all of them, leveraging computational efficiency. A can be factorized by SVD as [33]
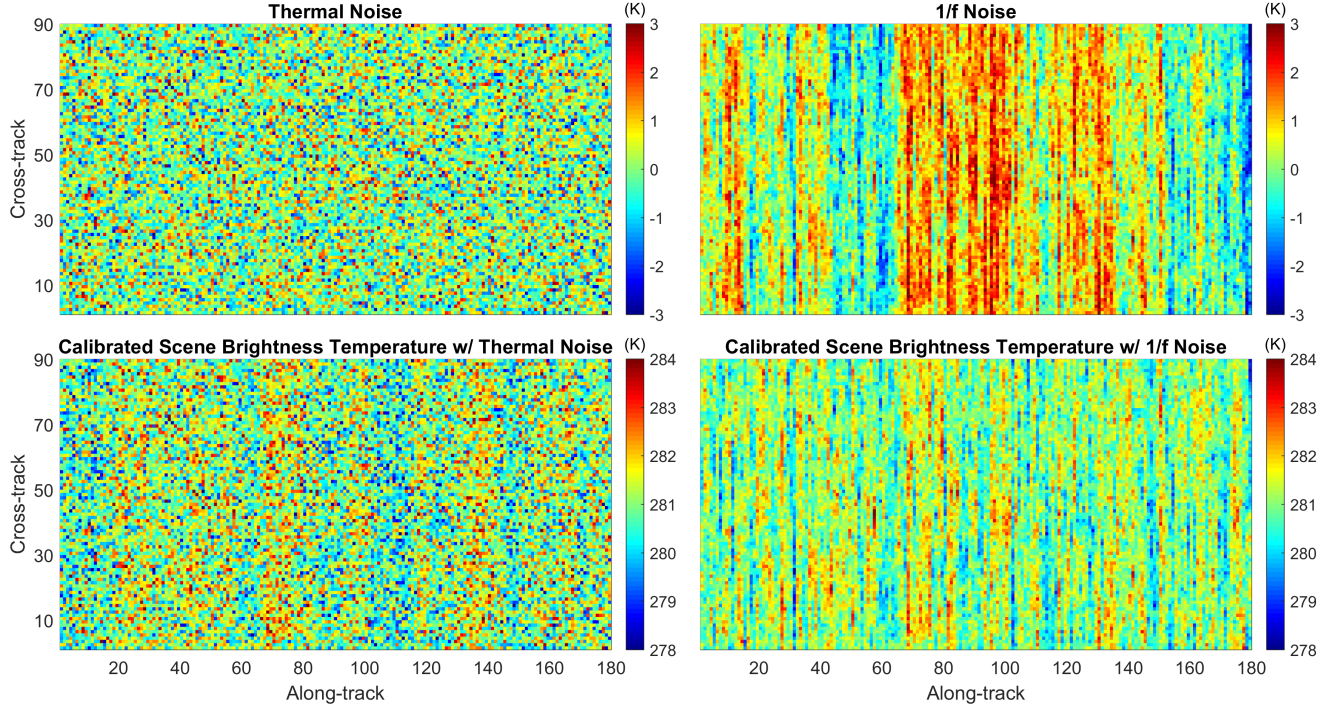
$$A = USV^T \tag{28}$$

Fig. 4. A swath of thermal noise and $1/f$ noise and their impact on the scene brightness temperature. (Upper left) Thermal noise shows no difference between cross-track and along-track. (Upper right) In contrast, $1/f$ noise has remarkable cross-track stripes that are sharp and non-periodic, and the mean oscillates along-track. In the meantime, both thermal and $1/f$ noise produce stripes in the scene T_B, which exhibit different features. (Lower right) For T_B with $1/f$ noise, the along-track fluctuation is removed through the periodic calibration, but the cross-track stripes remain. (Lower left) With regard to T_B with thermal noise, moderate cross-track bands show up. These bands are smoother without sharp edges but span over each cross-track scanline. They are due to the periodic calibration, where the derived power gains are affected by noise and are applied to the entire cross-track samples.

where U is an $m \times n$ orthogonal matrix, V is an $n \times n$ orthogonal matrix, and S is an $m \times n$ rectangular diagonal matrix with nonnegative diagonal entries. The diagonal entries of S are singular values of A. We can define S^2 as

$$S^2 = S^T S = \begin{bmatrix} \sigma_1^2 & 0 & \dots & 0 \\ 0 & \sigma_2^2 & \dots & 0 \\ \vdots & \vdots & \ddots & 0 \\ 0 & 0 & \dots & \sigma_n^2 \end{bmatrix} \quad (29)$$

where S^2 can be sorted with the diagonal entries from high to low such that $\sigma_1 \geq \sigma_2 \geq \dots \geq \sigma_n$.

SVD is related to eigen-decomposition as

$$\begin{aligned} A^T A &= (USV^T)^T (USV^T) \\ &= V S^T U^T U S V^T \\ &= V S^T I S V^T \\ &= V S^2 V^T \end{aligned} \quad (30)$$

Combining Equations 25-29, there are $\Lambda = \frac{1}{(n-1)} S^2$ and $E = V$. Λ can be written as

$$\Lambda = \begin{bmatrix} \lambda_1 & 0 & \dots & 0 \\ 0 & \lambda_2 & \dots & 0 \\ \vdots & \vdots & \ddots & 0 \\ 0 & 0 & \dots & \lambda_n \end{bmatrix} \quad (31)$$

where $\lambda_i = \frac{1}{(n-1)} \sigma_i^2$.

The projection of A onto the eigenvector basis is

$$P = AV \quad (32)$$

where P is an $n \times n$ matrix with the columns of P as the principal components (PCs). For the ith PC, the corresponding variance is λ_i.

The explained variance can be written in ratio by normalization

$$R_{var}(i) = \frac{\lambda_i}{\sum_i^m \lambda_i} \quad (33)$$

The cumulative explained variance ratio is the discrete integration of $R_{var}(i)$.

III. RESULTS

A. Simulation

We have examined how the thermal and $1/f$ noise are related to striping. Figure 4 shows the two noises of 1-K standard deviation and their impact on the calibrated scene temperature. In the upper panels, thermal noise shows no difference between cross-track and along-track. In contrast, $1/f$ noise has cross-track stripes. The stripes are sharp and non-periodic with significant fluctuation. They are not constant in each individual cross-track scanline. This is different from stripes observed in many visible and infrared sensors, which show constant cross-track stripes [34], [35]. In the along-track direction, $1/f$ noise shows fluctuation with non-stationary mean, which differs from that of thermal noise.
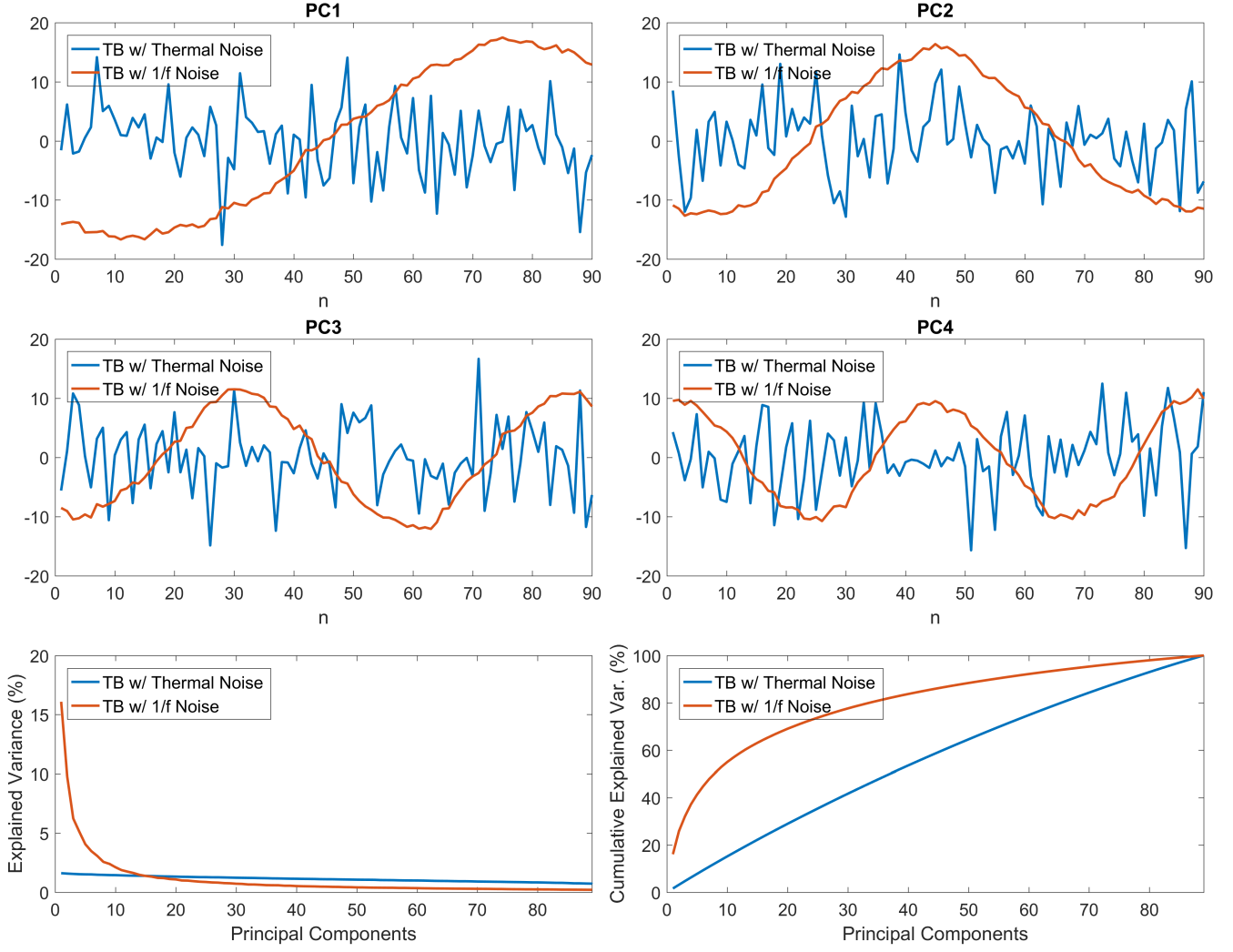
Fig. 5. PCA analysis for T_B with thermal and $1/f$ noise in lower panels of Figure 4. For T_B with thermal noise, the first four PCs show characteristics of white noise without noticeable difference between them. PCs with $1/f$ noise are like Fourier series with sinusoidal shapes and periods. Their frequencies increase by 0.5 times along the PC sequence. The explained variance and its cumulation are shown. The explained variance is very flat for T_B with thermal noise. With $1/f$ noise, the first few PCs stand out, and the rest of the PCs decrease till converging to the background noise floor. The first ten PCs account for 55% and 15% of total variance for T_B with $1/f$ and thermal noise, respectively.

The calibrated scene T_B with thermal and $1/f$ noise is illustrated in the lower panels in Figure 4. A uniform scene target of 281 K is used in the simulation, which is close to the average warm-load temperature of MetOp-A MHS. For T_B with $1/f$ noise, the along-track fluctuation is reduced. This is because of the periodic calibration that can capture the fluctuation, to some degree. However, the sharp cross-track stripes are retained.

Unexpectedly, moderate stripes are found in T_B with thermal noise. The stripes exhibit different features from that of $1/f$ noise. They look smoother with no sharp edges. In the along-track direction, there are moderate fluctuations that are relatively wide. They can be described as bands with wider and smoother features rather than narrow and sharp stripes.

It turns out that the thermal-noise induced bands arise from the periodic calibration that processes count to T_B. The gain is derived from the cold and warm references. For MHS, seven scans are averaged to calculate the gain in the operational algorithm [12]. A constant gain is applied to all scans in one cross-track line. The fluctuation of thermal noise propagates to gain and then the T_B. The bands fluctuation is a function of the calibration averaging window that is implemented. In summation, both thermal and $1/f$ noise generate bands/stripes but with different features. They are blended together in practice. Stripes due to $1/f$ noise are dominant.

We further decompose the striped T_B with PCA. T_B with thermal and $1/f$ noise in Figure 4 is decomposed to a set of PCs. The T_B matrix for PCA decomposition has a size of 90×180. The first four PCs are shown in Figure 5. The PCs of T_B with thermal noise show characteristic of white noise. However, PCs with $1/f$ noise have clear periodicity similar to the Fourier series. The first PC has the maximum variance with half cycle of one sinusoid. The second PC has a frequency increased by 0.5 times, and so are the rest of PCs.
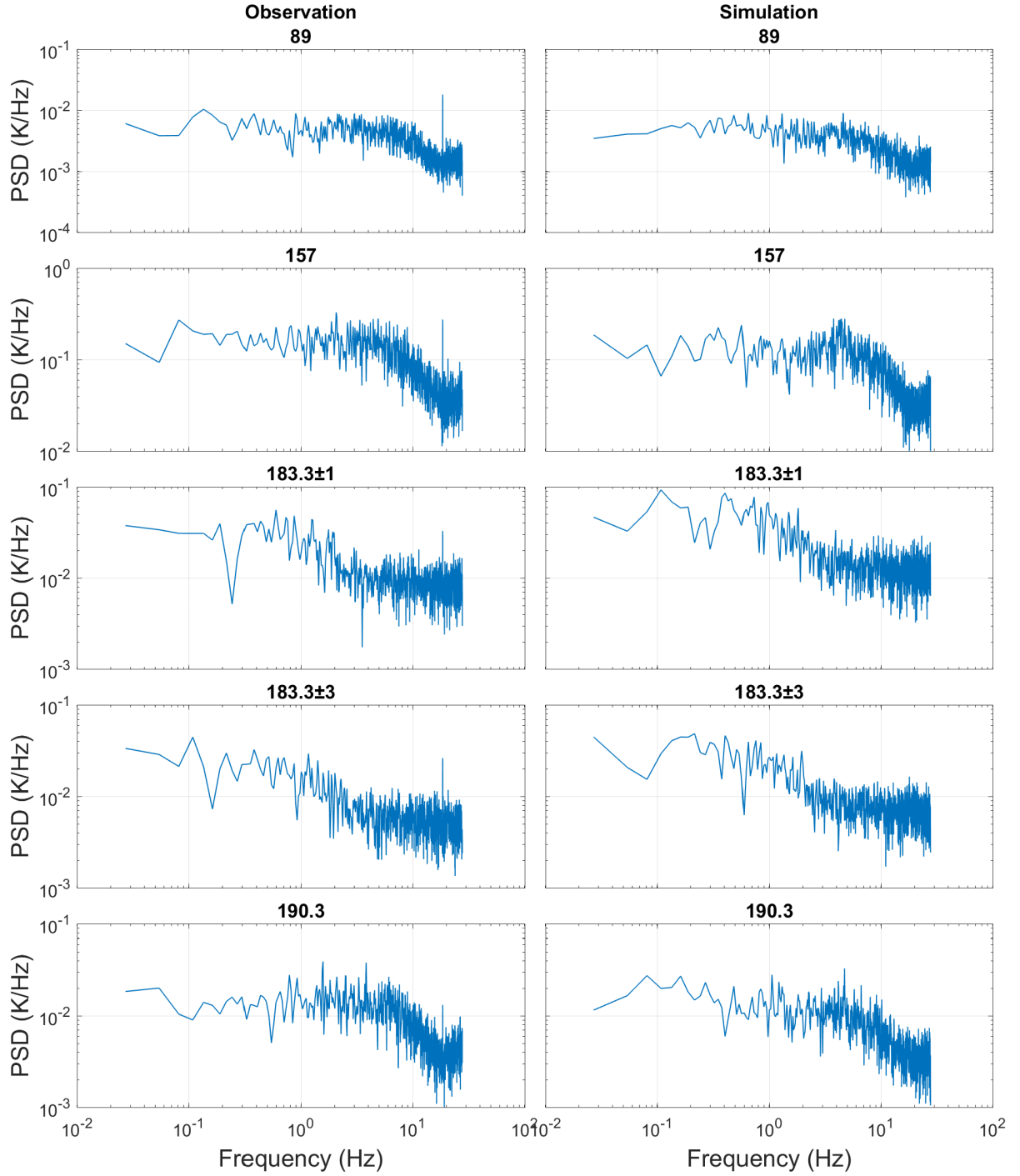
Fig. 6. PSDs of observation and simulation on July 1st, 2019. All PSDs illustrate the presence of $1/f$ noise in low-frequency regimes. There is a notable difference between these PSDs. For channels 89, 157, and 190.3 GHz, their PSDs illustrate more significant $1/f$ noise with larger bumps covering the range from 6 to 20 Hz. Channels of $183.31 \pm 1/3$ have more thermal noise, while $1/f$ noise is present below 5 Hz. The simulation reproduces noise characteristics as observation.
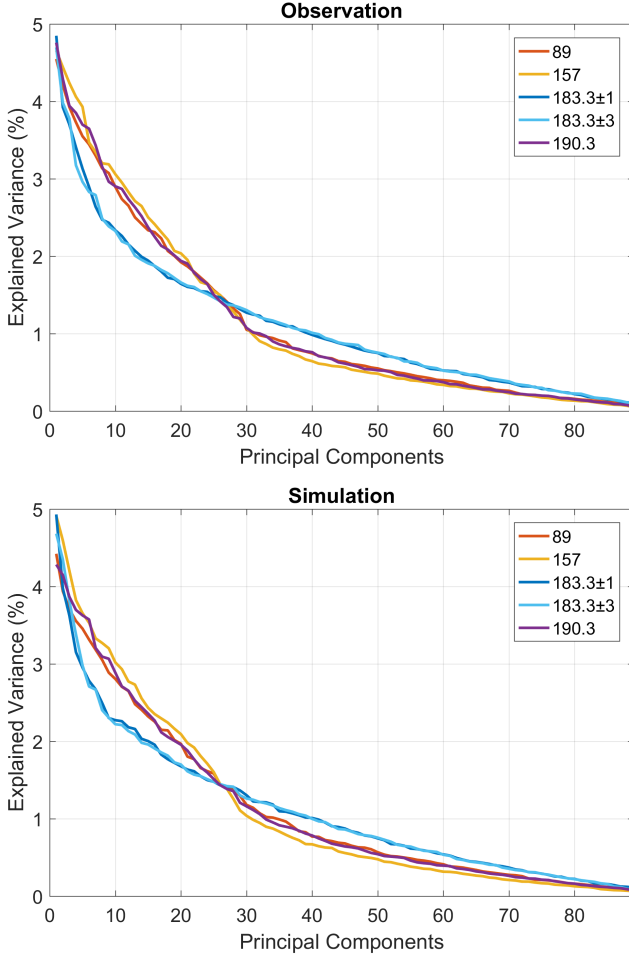
Fig. 7. Explained variance of observation and simulation. All the curves tilt up with the first few PCs standing out against the background floor, indicating the presence of $1/f$ noise. The curves have two families with a clear intersection between them. Before the intersection, the magnitudes of the first few PCs are larger for channels 89, 157, and 190.3 GHz than that of $183.31 \pm 1/3$ GHz. This indicates more $1/f$ noise of the three channels. The results are consistent with PSD analysis.

The explained variance is very flat for T_B with thermal noise. For T_B with $1/f$ noise, the first few PCs stand out against the background noise, and the rest of them converge to the background noise floor. According to the cumulative explained variance, the first ten PCs explains 55% of the total variance and 15% for T_B with $1/f$ and thermal noise, respectively.

The decomposition offers a new perspective for assessing the impact of $1/f$ and thermal noise and validating the simulation. The low-frequency regime of $1/f$ noise matters in producing the large fluctuation. The first few PCs have relatively long periods and large variance against the background noise floor, which result in large fluctuation and are the primary driver of striking stripes. Additionally, the decomposition is useful for estimating the 1/f significance with the explained variance and validating simulation against observation, as we will find in next section.

B. Observation and simulation

We have examined the striping of MetOp-A MHS with both observation and simulation. MHS 157 GHz has shown degradation since November 2018. For instance, striking striping is noticeable in the dynamic scene T_B on July 1st, 2019, shown in Figure 1. However, the striping detected with a high-pass filter still has large residual uncertainties, and accurately striping quantification is impossible. We have extracted the striping from the warm-load $T_{A,W}$ with the method we developed. In accordance with the observation, we have done simulation and generated the $T_{A,W}$ in the same way.

Figure 6 shows the striping PSD of observation and simulation. $T_{A,W}$ only has 3 cross-track samples, and thus it is better to compare the striping in the frequency domain rather than time domain. All PSDs illustrate the presence of $1/f$ noise in the low-frequency regime. Furthermore, we see a difference between channels in terms of their $1/f$ noise characteristics. Channels 89, 157, and 190.3 GHz show more significant $1/f$ noise with a larger bump in the PSD covering from 6 to 20 Hz. In contrast, channels $183.31 \pm 1/3$ have thermal noise spanning from 28 Hz to 5 Hz, and $1/f$ noise below 5 Hz.

The explained variance from PCA exhibits the channel difference shown in Figure 7. PCA is applied to warm-load noise $T_{A,W}$. The original $T_{A,W}$ is from two orbits of 3 cross-track samples and 5400 along-track scans with a total of 16200 measurements, which are reshaped to have 90 cross-track samples and 180 along-track scans to generate more PCs for better comparison. All channels show the presence of $1/f$ noise such that the first few PCs stand out against the background floor. We see an obvious difference between $183 \pm 1/3$ GHz and the other three channels of 89, 157, and 190 GHz. There is a clear intersection around PC 26th of the two types of channels. PCs are smaller before the intersection for $183 \pm 1/3$ GHz, indicating less $1/f$ noise. The results are consistent with PSD analysis. The explained variance is much less noisy than PSD and help discern the channel difference. The difference of observation and simulation has a bias of less than 0.04 K across all channels.

The results show that the algorithm we developed can identify striping regardless of the dynamics of scene T_B at W/G bands. Although only channel 157 GHz shows pronounced striping in the Earth scene T_B, the other channels also have striping, which is masked out in Earth scene T_B due to its large dynamic range. The simulation reproduces similar characteristics in all aspects as observation. Simulation suggests that $1/f$ noise is the primary cause for striping. The periodic calibration generates bands, but they have a different feature and are a secondary effect of striping. We will quantify the magnitude of striping in the next section.

C. Striping quantification, composition and variability

Figure 8 shows the quantification with degradation data on July 1st, 2019. For 157 GHz, NEDT of total noise is as high as 1.5 K, which is tripled its normal level of 0.5 K. NEDT of thermal and $1/f$ noise is 0.98 and 1.15 K, respectively. The striping percentage is 58%, corresponding to a striping ratio ($1/f$ over thermal) of 1.18. The index quantifies the
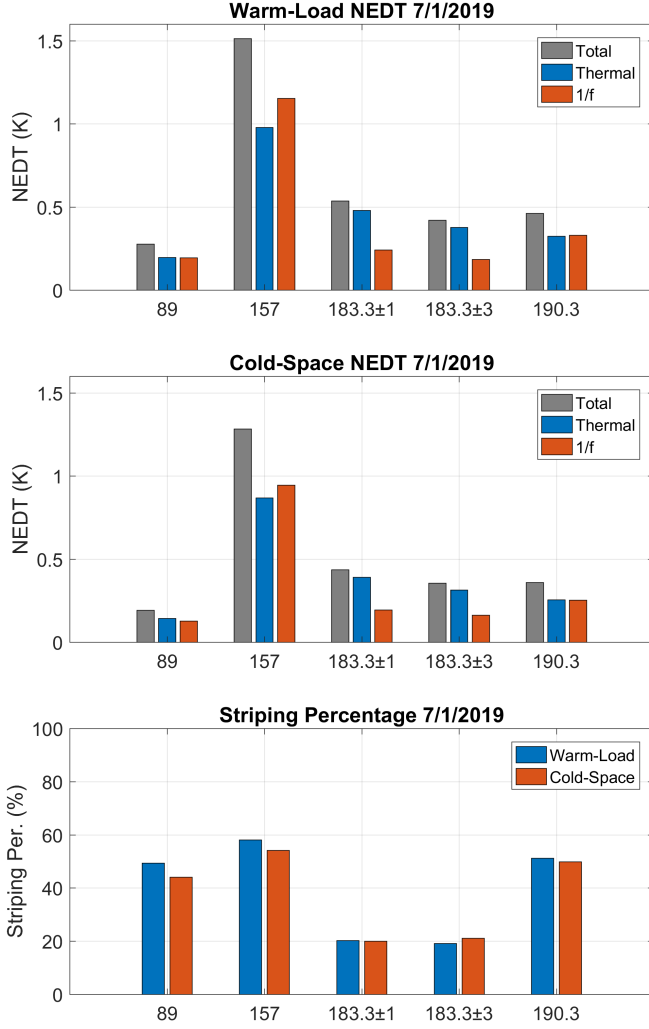
Fig. 8. Striping decomposition in terms of total, thermal and $1/f$ noise on July 1st, 2019. Channel 157 GHz has the largest absolute noise that is doubled its normal level. The striping percentage is similar for channels 89, 157, and 190.3 GHz, but lower for 183 GHz. This is consistent with PCA and PSD analyses. Both cold-space and warm-load scenes show consistent results. The absolute noise magnitudes are slightly smaller for the cold-space, but the striping percentage is almost the same with no dependence on the scene temperature.
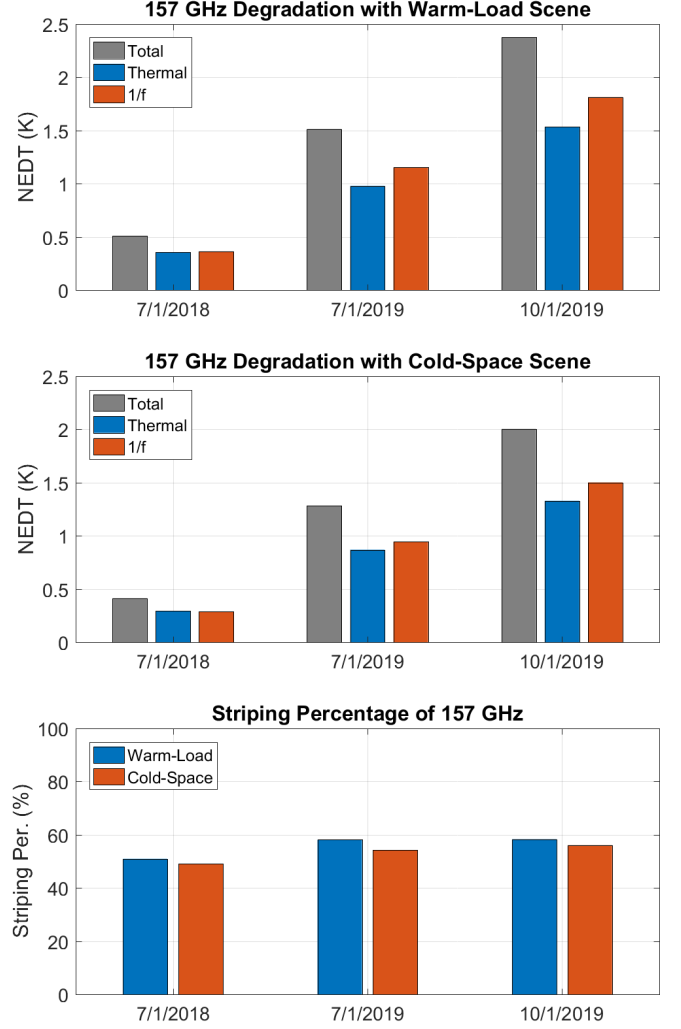
Fig. 9. The degradation of 157 GHz and its composition. Since its degradation in November 2018, the absolute magnitudes of the total, thermal and $1/f$ noise are nearly quadrupled by July and October 1st, 2019, respectively. However, the striping percentage does not change regardless of the degradation. Both cold-space and warm-load show consistent results.

NEDTs.

Figure 9 shows the degradation of 157 GHz on different days. Degradation took place around November 2018. On July 1st, 2018, this channel functions normally. We observe a severe degradation with NEDT nearly tripled and quadrupled in July and October of 2019, respectively. The increase is for all the total, thermal and $1/f$ noise. Both cold and warm scenes see consistent degradation. In the meantime, the striping percentage remains the same. This suggests the degradation arise from both thermal and $1/f$ noise with their striping ratio remaining the same.

The time series of all channels are shown in Figure 10. The degradation of channel 157 GHz is significant since November 2018. The noise including total, thermal and $1/f$ increased remarkably. Meanwhile, the striping percentage is the same with only a slight increase. The other channels illustrate stable noise level and striping percentage. The striping percentage

significance of striping. The other four channels show normal NEDTs of total noise below 0.5 K. However, very high striping percentages are also found for channels 89 and 190 GHz, which are 49% and 51%, respectively. This is in contrast to the channels of $183.31 \pm 1/3$ that have relatively low striping percentages of 24% and 18%, respectively.

We have examined the striping dependence on the scene temperature with both warm-load and cold-space T_B. Both cold and warm scenes have consistent striping in terms of total, thermal, striping percentage. For 157 GHz, the striping percentage is very close for the cold-space and warm-load. This suggests that $1/f$ and thermal noise has a constant ratio independent of scene dependence. The absolute magnitudes show moderate scene dependence with the noise ratio of cold-space to warm-load around 80% for all total, thermal, and $1/f$
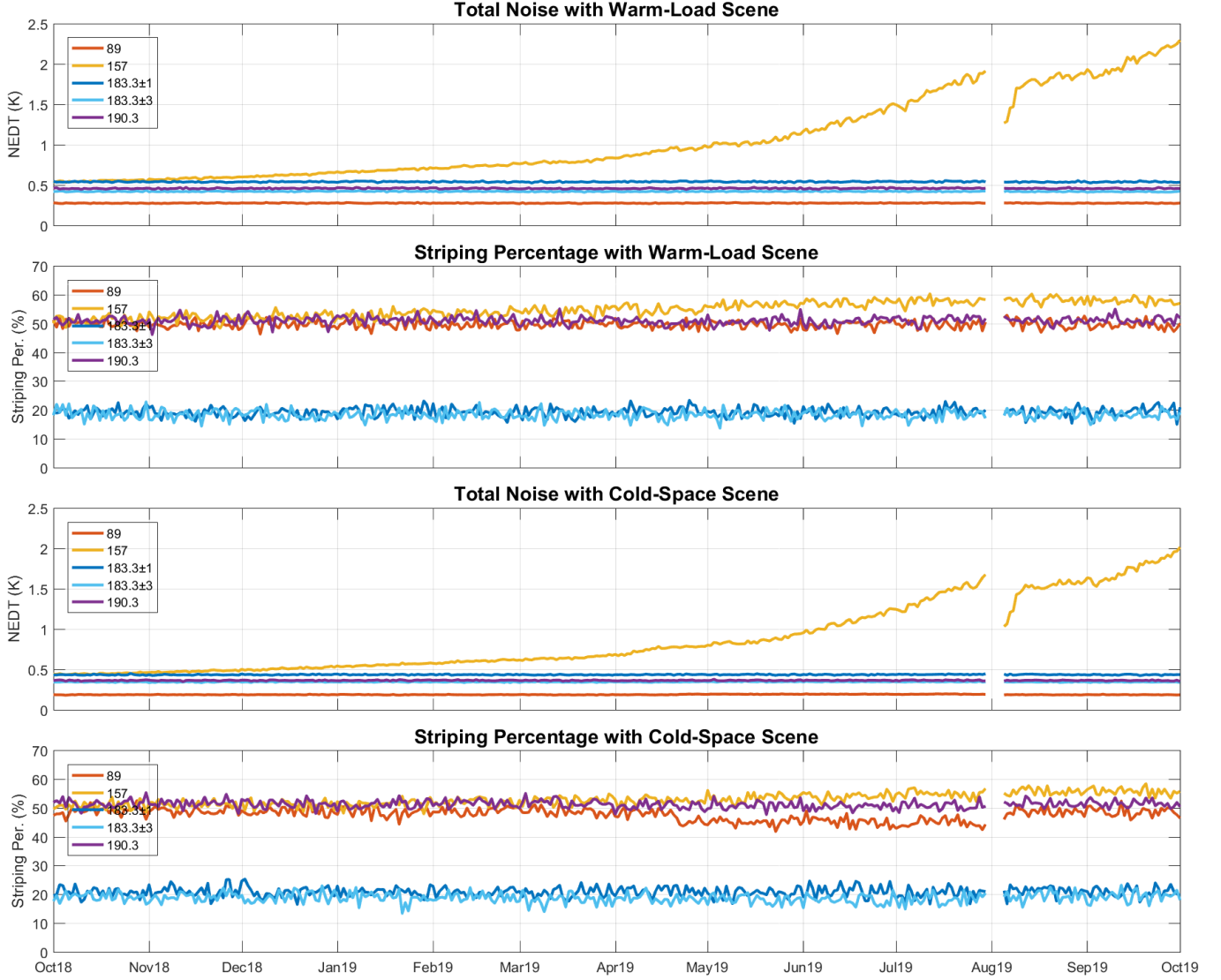
Fig. 10. Time series of MetOp-A MHS from October 2018 to October 2019. Channel 157 GHz has degraded since November 2018 as found in both cold and warm scenes. While the noise at 157 GHz raises up for the total, thermal and $1/f$ noise, the striping percentage remains almost the same. The other channels also show stable striping percentages. A data outage occurred from July 30 to August 4, 2019 that affected all instruments on MetOp-A.

shows no dependence on the scene temperature according to the cold and warm measurements. There is a moderate scene dependence for the absolute noise magnitude. A data outage took place on July 30th, 2019 and persisted for few days till August 5th. The outage affected all payloads on MetOp-A. We observed that the noise at 157 GHz dropped after the outage but quickly raised up again.

D. Earth-scene striping from empirical simulation

Although remarkable striping is observed for 157 GHz channel in Figure 1, the residual uncertainties remains too large for an accurate quantification. Generating striping is needed for assessing its propagation and impact through science products, data assimilation, and NWP modeling. We have derived empirical parameters from the warm-load and cold-space and performed simulation. The validation is done by comparing simulation against observation in previous sections.

We simulate the striping for the Earth scene with the empirical parameters. Since there is no strong scene dependence, we apply the empirical parameters of warm-load to simulate Earth scene striping.

Figure 11 shows the simulated Earth scene striping on July 1st, 2019. We only present 157 and 183 GHz since they represent two families of striping with severe and moderate degrees, respectively. The striping ratio is over 1 for the severe group, while less than 0.5 for the moderate ones. Noticeable striping is seen at channel 157 GHz. The striping has large magnitudes ranging from -5 to 5 K. 183 GHz also shows striping but with less significance. Since the exact striping profile cannot be accurately extracted from the earth scene data, the simulation provides a substitute for quantifying and propagating its effect through the NWP modeling and science data products.
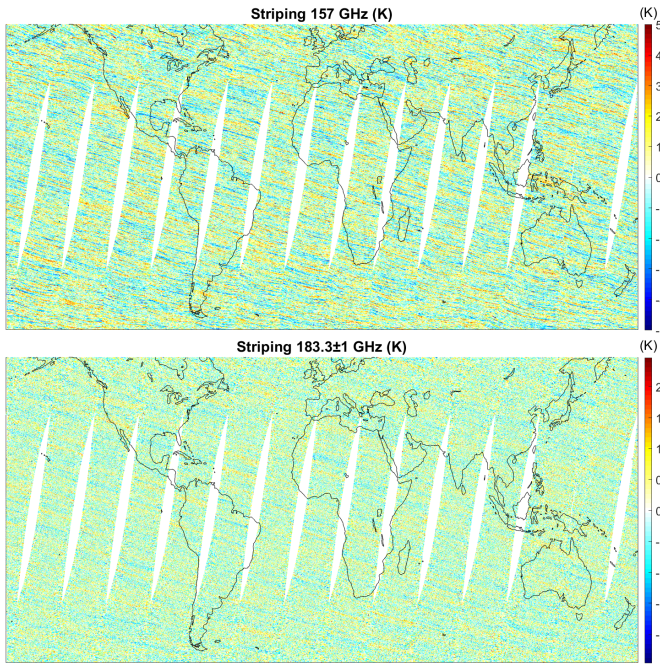
Fig. 11. Striping in Earth scenes from empirical simulation on July 1st, 2019. Empirical parameters include magnitudes of thermal, $1/f$ noise, and orbital oscillation based on observation. Channel 157 GHz has more significant striping than that of 183 GHz. The simulation complements observation in Figure 1, where we see the striping but the accurate quantification is impossible due to large uncertainties. With the empirical simulation, striping can be produced and used for quantifying its impact on NWP modeling and science products.

IV. CONCLUSION AND DISCUSSION

Severe striping has been observed for MetOp-A MHS, but accurate striping quantification is still challenging due to the large Earth scene dynamics at W/G bands. In this study, we have developed a set of novel algorithms for striping quantification, decomposition, characterization, and simulation. Rather than dealing with the dynamical Earth scenes, our algorithms utilize the cold-space and warm-load scenes that are stable with the striping information of a high signal-to-noise ratio. MHS striping and its composition are revealed and quantified, and our simulation can reproduce striping characteristics against observation.

We find that $1/f$ noise can produce cross-track striping that is sharp and non-periodic with large fluctuation. Stripes are not constant for each cross-track scanline. In the along-track direction, fluctuation is also present due to the non-stationary mean of $1/f$ noise. The periodic calibration reduces the fluctuation along-track, but cross-track stripes are retained. In the meantime, cross-track bands arise from the periodic calibration, even in the presence of only thermal noise. These bands are smoother with smaller magnitudes. They are due to the derived gain that is periodic and affected by noise. In practice, bands and stripes from thermal and $1/f$ noise are blended, and the latter is more significant. With PCA decomposition, the first few PCs of T_B stand out against the background noise floor, showing sinusoidal and periodic oscillation cross-track. They are dominant in causing striping.

We quantify the striping and decompose it into two parts of thermal and $1/f$ noise. The total, thermal and $1/f$ noise of 157 GHz had nearly tripled and quadrupled by July and October 2019, respectively, compared to its normal level. The striping percentage remains the same regardless of the degradation. This indicates that degradation has occurred for both thermal and $1/f$ noise with their ratio locked. In addition to 157 GHz, the other four channels also show the presence of striping. Channels 89 and 190 GHz are found to have the same level of striping percentage of over 50% as 157 GHz. The two 183-GHz channels show a lower striping percentage of around 20%. The striping is present in both cold-space and warm-load observations. The absolute magnitude of noise and striping are slightly higher in the warm-load scenes than in the cold-space, while the striping percentage shows no scene dependence.

The results provide insights for quantifying striping of MHS and understanding its characterization and cause. It does not escape our attention that our algorithms can be applied to other radiometers. Our methods allow for quantifying and comparing striping in terms of the absolute magnitude and relative ratio among different radiometers. Our simulation model can be applied for studying the observation error propagation in data assimilation, NWP modeling, and science products.

REFERENCES

[1] L. K. Vandamme, "Noise as a Diagnostic Tool for Quality and Reliability of Electronic Devices," *IEEE Transactions on Electron Devices*, 1994.

[2] R. F. Jarnot, "Calibration of the Microwave Limb Sounder on the Upper Atmosphere Research Satellite," *Journal of Geophysical Research Atmospheres*, 1996.

[3] N. Garmendia and J. Portilla, "Investigations of AM, PM noise, and noise figure in an SiGe-HBT amplifier operating in linear and nonlinear regimes," *IEEE Transactions on Microwave Theory and Techniques*, 2010.

[4] E. Kim, C. H. J. Lyu, K. Anderson, R. Vincent Leslie, and W. J. Blackwell, "S-NPP ATMS instrument prelaunch and on-orbit performance evaluation," *Journal of Geophysical Research Atmospheres*, vol. 119, no. 9, pp. 5653–5670, 2014.

[5] N. Bormann, A. Fouilloux, and W. Bell, "Evaluation and assimilation of ATMS data in the ECMWF system," *Journal of Geophysical Research Atmospheres*, 2013.

[6] Z. Qin, X. Zou, and F. Weng, "Analysis of ATMS striping noise from its Earth scene observations," *Journal of Geophysical Research Atmospheres*, 2013.

[7] J. Li and G. Liu, "Direct assimilation of Chinese FY-3C Microwave Temperature Sounder-2 radiances in the global GRAPES system," *Atmospheric Measurement Techniques*, 2016.

[8] D. Gu, "ATMS Striping Assessment and Mitigation," NGAS SNPP Mission Support Team, Tech. Rep., 2013. [Online]. Available: https://www.star.nesdis.noaa.gov/star/

[9] A. Collard, J. Derber, R. Treadon, N. Atkinson, J. Jung, and K. Garrett, "Toward assimilation of CrIS and ATMS in the NCEP Global Model," in *Proc. 18th Int. TOVS Study Conf., Toulouse, France, International TOVS Working Group*, vol. 1, 2012.

[10] T. Janjić, N. Bormann, M. Bocquet, J. A. Carton, S. E. Cohn, S. L. Dance, S. N. Losa, N. K. Nichols, R. Potthast, J. A. Waller, and P. Weston, "On the representation error in data assimilation," *Quarterly Journal of the Royal Meteorological Society*, vol. 144, no. 713, pp. 1257–1278, 2018.

[11] T. Popp, M. I. Hegglin, R. Hollmann, F. Ardhuin, A. Bartsch, A. Bastos, V. Bennett, J. Boutin, C. Brockmann, M. Buchwitz *et al.*, "Consistency of satellite climate data records for earth system monitoring," *Bulletin of the American Meteorological Society*, vol. 101, no. 11, pp. E1948–E1971, 2020.

[12] J. Robel and A. Graumann, "NOAA KLM User's Guide with NOAA-N, N Prime, and MetOp Supplements," Tech. Rep., 2014.

[13] J. X. Yang, D. S. McKague, and C. S. Ruf, "Uncertainties in radiometer intercalibration associated with variability in geophysical parameters," *Journal of Geophysical Research: Atmospheres*, vol. 121, no. 19, pp. 11–348, 2016.

[14] N. Bormann and P. Bauer, "Estimates of spatial and interchannel observation-error characteristics for current sounder radiances for numerical weather prediction. I: Methods and application to ATOVS data," *Quarterly Journal of the Royal Meteorological Society*, 2010.

[15] V. O. John, G. Holl, S. A. Buehler, B. Candy, R. W. Saunders, and D. E. Parker, "Understanding intersatellite biases of microwave humidity sounders using global simultaneous nadir overpasses," *Journal of Geophysical Research: Atmospheres*, vol. 117, no. D2, 2012.

[16] K. M. Newman, C. S. Schwartz, Z. Liu, H. Shao, and X. Y. Huang, "Evaluating forecast impact of assimilating microwave humidity sounder (MHS) radiances with a regional ensemble Kalman filter data assimilation system," *Weather and Forecasting*, 2015.

[17] W. J. Blackwell, S. Braun, R. Bennartz, C. Velden, M. DeMaria, R. Atlas, J. Dunion, F. Marks, R. Rogers, B. Annane, and R. V. Leslie, "An overview of the TROPICS NASA Earth Venture Mission," *Quarterly Journal of the Royal Meteorological Society*, 2018.

[18] S. Padmanabhan, T. C. Gaier, A. B. Tanner, S. T. Brown, B. H. Lim, S. C. Reising, R. Stachnik, R. Bendig, and R. Cofield, "TEMPEST-D Radiometer: Instrument Description and Prelaunch Calibration," *IEEE Transactions on Geoscience and Remote Sensing*, 2020.

[19] T. H. Lee, *The Design of CMOS Radio-Frequency Integrated Circuits*. Cambridge Univ, 2004.

[20] W. A. Davis and K. K. Agarwal, *Radio Frequency Circuit Design*, 2nd ed. New York: Wiley, 2011.

[21] M. S. Hersman and G. A. Poe, "Sensitivity of the Total Power Radiometer with Periodic Absolute Calibration," *IEEE Transactions on Microwave Theory and Techniques*, vol. 29, no. 1, pp. 32–40, 1981.

[22] M. A. Goodberlet and J. B. Mead, "Two-Load Radiometer Precision and Accuracy," *IEEE Transactions on Geoscience and Remote Sensing*, 2006.

[23] J. X. Yang and D. S. McKague, "Improving collocation-based scan-dependent intercalibration over the ocean for spaceborne radiometry," *IEEE Geoscience and Remote Sensing Letters*, vol. 13, no. 4, pp. 589–593, 2016.

[24] F. Ulaby and D. Long, *Microwave Radar and Radiometric Remote Sensing*. Univ. of Michigan Press, 2014.

[25] S. A. Kassam and J. B. Thomas, *Signal Detection in Non-Gaussian Noise*. Springer, 2012.

[26] M. Matsumoto and T. Nishimura, "Mersenne Twister: A 623-Dimensionally Equidistributed Uniform Pseudo-Random Number Generator," in *ACM Transactions on Modeling and Computer Simulation*, 1998.

[27] W. J. Riley, "NIST Special Publication 1065 Handbook of Freequency Stability Analysis," *International Journal of Rock Mechanics and Mining Science*, 2008.

[28] J. X. Yang and H. Yang, "A New Algorithm for Determining the Noise Equivalent Delta Temperature of In-Orbit Microwave Radiometers," *IEEE Transactions on Geoscience and Remote Sensing*, 2021.

[29] P. W. Gaiser, K. M. St. Germain, E. M. Twarog, G. A. Poe, W. Purdy, D. Richardson, W. Grossman, W. L. Jones, D. Spencer, G. Golba, J. Cleveland, L. Choy, R. M. Bevilacqua, and P. S. Chang, "The windSat spaceborne polarimetric microwave radiometer: Sensor description and early orbit performance," *IEEE Transactions on Geoscience and Remote Sensing*, 2004.

[30] J. X. Yang, D. S. McKague, and C. S. Ruf, "Identifying and resolving a calibration issue with gmi," in *2015 IEEE International Geoscience and Remote Sensing Symposium (IGARSS)*. IEEE, 2015, pp. 2568–2571.

[31] J. R. Piepmeier, P. Focardi, K. A. Horgan, J. Knuble, N. Ehsan, J. Lucey, C. Brambora, P. R. Brown, P. J. Hoffman, R. T. French, R. L. Mikhaylov, E. Y. Kwack, E. M. Slimko, D. E. Dawson, D. Hudson, J. Peng, P. N. Mohammed, G. De Amici, A. P. Freedman, J. Medeiros, F. Sacks, R. Estep, M. W. Spencer, C. W. Chen, K. B. Wheeler, W. N. Edelstein, P. E. O'Neill, and E. G. Njoku, "SMAP L-Band Microwave Radiometer: Instrument Design and First Year on Orbit," *IEEE Transactions on Geoscience and Remote Sensing*, 2017.

[32] J. Schoukens, R. Pintelon, and H. Van Hamme, "The interpolated fast fourier transform: A comparative study," *IEEE Transactions on instrumentation and measurement*, vol. 41, no. 2, pp. 226–232, 1992.

[33] C. D. Meyer, *Matrix analysis and applied linear algebra*. Siam, 2000, vol. 71.

[34] P. Rakwatin, W. Takeuchi, and Y. Yasuoka, "Stripe noise reduction in MODIS data by combining histogram matching with facet filter," *IEEE Transactions on Geoscience and Remote Sensing*, 2007.

[35] C. Cao, F. J. De Luccia, X. Xiong, R. Wolfe, and F. Weng, "Early on-orbit performance of the visible infrared imaging radiometer suite onboard the suomi national polar-orbiting partnership (S-NPP) satellite," *IEEE Transactions on Geoscience and Remote Sensing*, 2014.
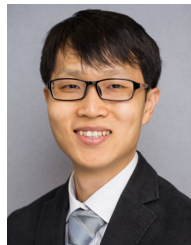
John Xun Yang (Senior Member, IEEE) received the Ph.D. degree from the University of Michigan, Ann Arbor, MI, USA, in 2015.

He is an Assistant Research Scientist with the Earth System Science Interdisciplinary Center (ESSIC) and the Cooperative Institute for Satellite Earth System Studies (CISESS) at University of Maryland. His research interests include Earth remote sensing, microwave radiometry. He has been involved with several NASA/NOAA satellite missions. He is a member of the NASA/JAXA Global Precipitation Measurement (GPM) mission and works on satellite radiometer calibration and science applications. He has done engineering work on building up an L-band radiometer and accessory data acquisition system to calibrate GPS simulators for the NASA Cyclone Global Navigation Satellite System (CYGNSS) mission. He did multiple field campaigns for the NASA Aquarius mission. He is a member of NOAA/NASA Joint Polar Satellite System (JPSS) mission with focus on the Advanced Technology Microwave Sounder (ATMS).

He has chaired the ESSIC Seminar Series and invited outstanding scientists to deliver talks on Earth interdisciplinary studies since 2018. Among the speakers are members and fellows of IEEE/AMS/AGU, the US National Academies members, and the Nobel Prize winners. He has served as an associate editor for *IEEE Access*. Dr. Yang was a recipient of the first place prize at the 2013 Michigan Geophysical Union (MGU) Symposium, the ten finalists in the student paper contest of the 2015 International Geoscience and Remote Sensing Symposium (IGARSS), the 2016 NASA Science Team Award in Precipitation Measurement Mission (PMM) for working with GPM XCal calibration, and the 2019 ESSIC Service Award.
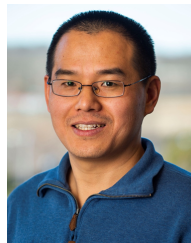
Yalei You received the B.S. and M.S. degrees in atmospheric science from Yunnan University, Kunming, Yunnan, China, in 2005 and 2008, respectively, and the Ph.D. degree in meteorology from Florida State University, Tallahassee, FL, USA, in 2013.

He is currently an Associate Research Scientist with the Earth System Science Interdisciplinary Center (ESSIC) and the Cooperative Institute for Satellite Earth System Studies (CISESS)-Maryland, University of Maryland (UMD), College Park, MD, USA. His research interests include passive microwave precipitation algorithm development, precipitation data set validation, and microwave instrument calibration. Dr. You has served as an Associate Editor for the *Journal of Hydrometeorology* and the *Journal of Applied Meteorology and Climatology*.

William Blackwell (Fellow, IEEE) is the Associate Leader of the Applied Space Systems Group at MIT Lincoln Laboratory, where he leads a number of projects involving atmospheric remote sensing, including the development and calibration of airborne and space-borne microwave sensors, the retrieval of geophysical products from remote radiance measurements, and the application of electromagnetic, signal processing, and estimation theory.

Dr. Blackwell has served as associate editor of the IEEE Transactions on Geoscience and Remote Sensing and the IEEE Geoscience and Remote Sensing Society (GRSS) Magazine, co-chair of the IEEE GRSS Remote Sensing Instruments and Technologies for Small Satellites working group, and has served on the NASA Aqua science team, and the National Academy of Sciences Committee on Radio Frequencies. He is currently the principal investigator on the NASA TROPICS Earth Venture mission. He was previously the Integrated Program Office sensor scientist for the Advanced Technology Microwave Sounder on the Suomi National Polar Partnership launched by NOAA in 2011 and the Atmospheric Algorithm Development team leader for the National Polar-orbiting Operational Environmental Satellite System (NPOESS) Microwave Imager/Sounder.

Dr. Blackwell received the MIT Lincoln Laboratory Technical Excellence Award in 2019 for his "innovative contributions to the science and practice of environmental monitoring." He was selected as a 2012 recipient of the IEEE Region 1 Managerial Excellence in an Engineering Organization Award "for outstanding leadership of the multidisciplinary technical team developing innovative future microwave remote sensing systems." In 2009, he was presented with the NOAA David Johnson Award for his work in neural network geophysical parameter retrievals and microwave calibration and is coauthor of "Neural Networks in Atmospheric Remote Sensing" (Artech House, 2009) and "Microwave Radar and Radiometric Remote Sensing" (Artech House, 2015). Dr. Blackwell has also been an author of more than 180 publications related to atmospheric remote sensing. He is a Fellow of the IEEE and an Associate Fellow of the AIAA.

Dr. Blackwell received the BEE degree in electrical engineering from the Georgia Institute of Technology and the SM and ScD degrees in electrical engineering and computer science from MIT, where he was a National Science Foundation Graduate Research Fellow.

Sidharth Misra (Senior Member, IEEE) received the B.E degree in electronics and communication engineering from Gujarat University, Ahmedabad, Gujarat, India, in 2004 and the M.S. degree in electrical engineering and computer science from the University of Michigan, Ann Arbor, in 2006. He received his Ph.D. degree in the Department of Atmospheric, Oceanic and Space Sciences, University of Michigan, Ann Arbor, in 2011.

He is currently a technologist at the NASA Jet Propulsion Laboratory in Pasadena, CA. He joined JPL in 2011 as a member of the Microwave Systems Technology group. He was a Research Engineer with the Space Physics Research Laboratory, University of Michigan and a Research Assistant with the Danish National Space Center, Technical University of Denmark (DTU), Lyngby. He was also with the Space Applications Center, Indian Space Research Organization, Ahmedabad.

His research interests include radio frequency interference algorithm development and mitigation, microwave radiometer system development and calibration. He was on the calibration team of the Aquarius radiometer, and was the instrument-scientist on the RACE mission. He was also the digital back-end lead for the CubeRRT mission. He is currently on the science team of SMAP, as well as Ocean Vector Winds for the COWVR mission, and radiometer calibration team member for the Juno microwave radiometer. He instrument manager for the PALS airborne system, and instrument scientist for the EZIE mission. He is a member of the Advisory Committee for the IEEE Geoscience and Remote Sensing Society (GRSS) and an Associate Editor for the GeoScience and Remote Sensing Letters. Dr. Misra is the recipient of the IGARSS 2006 Symposium Prize Paper Award, the 2009 IEEE-GRSS Mikio Takagi award and 2012 IEEE TGRS best reviewer award. He received a JPL Charles Elachi Early Career Award in 2016, a NASA Early Career Award in 2017, NASA Technical Achievement Award in 2019, and a JPL Lew Allen Award in 2020. Dr Misra has also received five NASA Group Achievement Awards.

Rachael A. Kroodsma received the B.S.E. degree in earth systems science and engineering, the M.S.E. degree in electrical engineering, and the Ph.D. degree in atmospheric, oceanic, and space sciences from the University of Michigan, Ann Arbor, MI, USA, in 2009, 2013, and 2014, respectively.

She is currently an Assistant Research Scientist with the Earth System Science Interdisciplinary Center, University of Maryland at College Park, College Park, MD, USA. She is also with the Precipitation Processing System at the NASA Goddard Space Flight Center, Greenbelt, MD, USA. She leads the Global Precipitation Measurement (GPM) Inter-Calibration Working Group (XCAL) and serves as Instrument Scientist for the airborne Conical Scanning Millimeter-wave Imaging Radiometer (CoSMIR) and Configurable Scanning Submillimeter-wave Instrument/Radiometer (CoSSIR). Her research interests include microwave radiometer calibration/intercalibration and remote sensing of the atmosphere from airborne and spaceborne sensors.